JOURNAL OF MATERIALS SCIENCE 32 (1997) 1639–1647

SAXS investigation of the structure of high-pressure crystallized poly(ethylene terephthalate): a new nanostructured material?

N. STRIBECK, H. G. ZACHMANN
Institut für Technologisch und Makromolekular Chemie, Universität Hamburg, Bundesstr. 45, D-20146 Hamburg, Germany

R. K. BAYER
Institut für Werkstofftechnik, Universität GH Kassel, Mönchebergstrasse 3, D-34109 Kassel, Germany

F. J. BALTÁ CALLEJA
Instituto de Estructura de la Materia, CSIC, Serrano 119, 28006 Madrid, Spain

The common crystallization conditions of poly(ethylene terephthalate) (PET) were replaced by an anabaric high-pressure crystallization at 320 °C. The PET samples were characterized by differential scanning calorimetry, density and microhardness. The resulting two-phase microstructure was studied by means of absolute small-angle X-ray scattering (SAXS). A complete SAXS analysis utilizing the interface distribution function (IDF) method was carried out. The resulting structure exhibited the presence of stacks of 10 nm thick crystalline lamellae which were separated by amorphous layers of about 1.3 nm thickness. Similar structures have been found after annealing of amorphous metals and have been termed nanocrystalline. Microhardness and structure have been discussed in analogy with the notions from the field of nanostructured materials. Theoretically, a multi-component lamellar two-phase structure has been discussed. The equations derived allow the computation of volume fractions and specific surfaces of the components (different kinds of stacks).

1. Introduction

In preceding studies, the structure of PET crystallized at atmospheric pressure from the amorphous state by small-angle X-ray scattering (SAXS) and its correlation to microhardness have been extensively investigated [1, 2]. Semicrystalline PET is known to form spherulites which are built from stacks of alternating crystalline lamellae and amorphous layers. Microhardness of PET crystallized isothermally under high pressure (4 kbar) has been recently determined to establish correlations with thermal properties and crystallinity [3]. The high crystallinities obtained for the high-pressure crystallized PET have been shown to give rise to unprecedently high microhardness values. Because measurement of the microhardness is frequently reported on nanostructured materials [4, 5], a comparison of the results obtained on high-pressure crystallized PET and those obtained on nanostructured materials is presented.

The search for substances with unusual properties is one of the challenges in the field of materials science. When one intends to achieve particularly high crystallinity in a polymer material like PET, in general one has to apply some sophisticated technique, because the nature of the polymer chains is known to restrict the degree of perfection under ordinary processing conditions. In the field of metallurgy, on the other hand, it usually requires considerable effort to transform a metallic compound into the amorphous or the semicrystalline state. Since the time when the advantages of imperfections were discovered by metallurgists, the formation of the so-called nanocrystalline state has become a widely discussed issue [4, 6–8] which has gained extra impetus after the discovery of the latest preparation technique: a transition of the material from the amorphous to the nanocrystalline state by annealing [9, 10]. A semicrystalline material is said to be nanocrystalline when its crystallites show dimensions of the order of 10–100 nm, and if the crystallites are separated by amorphous zones having thicknesses of only few atomic layers [4, 11].

Polymer precursors for the production of nanocrystalline ceramics as well as polymer matrices embedding various nanocrystalline materials have been reported

0022–2461

in the literature [12–20]. Interfaces between nanocrystalline alloys and polymers have also been studied. Recently, Nalwa *et al.* [21] were the first authors to report the fabrication of nano-size single crystals from polymers within a project which aims to produce electronic or photonic devices, similar to the main stream research in the field of nanostructured materials.

Small-angle X-ray scattering is well suited for studying the structure parameters of semicrystalline polymers. SAXS can be interpreted at different levels of complexity, the simplest one consisting of attributing a long period, L, to the position of the maximum observed in the scattering curve with the aid of Bragg's law [22]. In a two-phase structure, L is the sum of the average thickness of the crystalline lamellae, l_c, and the interlammellar regions, l_a. In many applications of SAXS it is of advantage to derive the correlation function from the observed intensity function [23]. The latter is related to the intensity function by Fourier transformation. Hence, all information which is hidden in the latter function, also is present in the observed correlation function. Finally, one can also calculate the interface distribution function, introduced by Ruland [24]. This function is the second derivative of the correlation function and represents the probability distribution of finding two interfaces – between a crystal and the neighbouring amorphous region – at a given distance. The advantage of this function is that it yields the average values of L, l_c, l_a and the distribution of the three quantities. In the Appendix, the basic aspects concerning the interface distribution and its calculation in case of a multicomponent lamellar system, are presented.

In the present paper we report the structure of high-pressure crystallized PET by means of SAXS in order to highlight the obtained results with reference to structures from nanocrystalline alloys and nanostructured compounds.

2. Experimental procedure

2.1. Materials preparation

High-crystallinity PET platelets with a diameter of 30 mm and a thickness of 2 mm were prepared in a hydraulic press. Amorphous PET pellets were melted in a cylindrical mould at a temperature of 275 °C for 35 min. Thereafter the melt was pressed at 500 bar. While holding the pressure, the temperature was decreased to 45 °C. The pressure was then increased up to 4 kbar and the temperature was raised to 320 °C. After 3 h the temperature was decreased to 45 °C within an interval of 10 min. Finally, the pressure was reduced to atmospheric pressure. In three consecutive runs, three samples were crystallized at high pressure. The physical properties of these samples are given in Table I. The preparation process entails a substantial loss of molecular weight. Viscosimetry shows an initial value $M_W = 30\,\mathrm{kg\,mol^{-1}}$, for the original material and a value of $M_W = 8\,\mathrm{kg\,mol^{-1}}$ for the high-pressure crystallized samples.

TABLE I Density, ρ, volume-crystallinity from density, α_D, melting temperature, T_m, volume crystallinity, from calorimetry, α_{cC}, and microhardness, H, of the high-pressure crystallized PET samples

	D55	D59	D63
ρ ($g\,cm^{-3}$)	1.4552 ± 10^{-4}	1.4586 ± 10^{-4}	1.4627 ± 10^{-4}
α_D	0.77	0.79	0.82
T_m (°C)	275	277	279
α_{cC}	0.89	0.84	0.87
H(MPa)	320	393	353

2.2. Techniques

Differential scanning calorimetry (DSC) measurements were carried out in the temperature range 25–300 °C at a heating rate of 10 °C min^{-1} by using a Mettler DSC 30 calorimeter. Crystallinity was determined from the ratio of the measured heat of fusion to the heat of fusion for infinitely thick crystals, $\Delta h_f = 135\,J\,g^{-1}$ [25].

The densities of the samples were measured in a density gradient column containing a mixture of CCl_4 and isopropanol. From every sample platelet, several pieces were measured. It turned out that the density is constant over the volume of all samples. Volume crystallinity, α_D, was computed from the density readings assuming $\rho_a = 1.338\,g\,cm^{-3}$ and $\rho_c = 1.490\,g\,cm^{-3}$ [26].

Microhardness was measured using a Leitz Durimet microhardness tester with a square-based pyramid indentor. The H-value was derived from the diagonal length of the indentation by using the relationship, $H = 1.854\,p/d^2$, where 1.854 is a geometrical factor, p is the applied force (N), and d is the diagonal length of the indentation (m). For each value of H, at least ten measurements of d were carried out, and the mean value was calculated [3]

Wide- and small-angle X-ray scattering patterns were recorded on photographic film using a pinhole camera, in order to ensure the isotropicity of the scattering patterns. For all X-ray measurements nickel-filtered CuK_α radiation was used. Quantitative SAXS measurements were carried out with a Kratky Compact Camera, equipped with proportional counter and energy discriminator. The receiving slit's length, l_1, was set to an integral length of 2.01 nm^{-1} in units of reciprocal space $\boldsymbol{s}$, $|\boldsymbol{s}|$ being defined as $(2/\lambda)\sin\theta$. (λ being the wavelength of radiation and θ half the scattering angle). Calibration to absolute intensity [27] was carried out by means of the moving slit method. Every scattering curve is composed of two parts, recorded with different entrance slit heights (50 and 110 μm), which overlap in the interval $s = 0.012$–$0.08\,nm^{-1}$. The resulting scattering curve covers the region between $s = 0.01$ and $1\,nm^{-1}$.

3. Data evaluation

Because data evaluation has been extensively discussed in previous papers [28, 29], only a short overview will be presented here. The raw data scattering curves from the Kratky camera were corrected for background scattering and calibrated in absolute

units. The region in which Porod's law is valid, was then searched and the quantities which describe the deviations of the observed two-phase system from an ideal one were determined. These quantities are the local density fluctuation background, $\tilde{I}_{Fl}/V$, and the thickness of the phase transition zone, d_t. The result is the smeared interference function of the ideal two-phase system, $\tilde{G}_{id}(s)$ (cf. Equation A1 of the Appendix). $\tilde{G}_{id}(s)$ was then transformed into the one-dimensional interface distribution function (IDF), $g_1(x)$, of the ideal two-phase lamellar system by using Equation A2 of the Appendix. The IDF was fitted with a model function using the Simplex algorithm. Several possible models were tested:

(i) a one-dimensional lattice of crystalline and amorphous regions, in which both the lattice constant and the thickness of the crystalline lamellae are subject to distortions;

(ii) an assembly of perfect lattices with different lattice constants; and

(iii) a one-dimensional stack with paracrystalline disorder [30–32] combined with the consideration of some asymmetry of the layer thickness distribution functions [28, 33].

It was found that model (iii) gives the best fitting results and therefore this model was applied in our evaluation. The fitting parameters were a weight factor, W, related to the amount of the interface per unit volume (cf. Appendix), the average thicknesses of amorphous and crystalline layers, $\bar{d}_a$ and $\bar{d}_c$, their relative variances, $\sigma_a/\bar{d}_a$ and $\sigma_c/\bar{d}_c$ and a parameter σ_H, which describes the skew of the distance distribution functions. If one knows the crystallinity of a sample from methods other than SAXS, one can easily identify which one of the average thicknesses is the crystalline one. Moreover, in previous studies [2, 28, 29] it was found that the relative width of the distribution of the crystalline thicknesses is, in general, the narrower one. Thus, by comparing the resulting values of $\sigma_a/\bar{d}_a$ with $\sigma_c/\bar{d}_c$, one is often able to distinguish between the crystalline and the amorphous layers only from the analysis of SAXS results.

4. Results

The macroscopic density, the melting temperature as determined by DSC, the volume fraction crystallinities from density and from DSC and the microhardness values of the samples investigated, are presented in Table I. The mass fraction crystallinity differs by less than 2% from the volume fraction crystallinity. The digits in the designation of the sample after the letter D denote the third and the fourth significant digit from the determined density.

Fig. 1 shows the slit-smeared small-angle X-ray scattering curves up to $s = 0.3\ nm^{-1}$. The presented data are corrected for background scattering and calibrated to absolute intensity. Close to $s = 0.08\ nm^{-1}$, one observes a well-developed maximum in the three curves. This value approximately corresponds to a long period of 12 nm. The integral scattering intensity increases with increasing density of the samples.

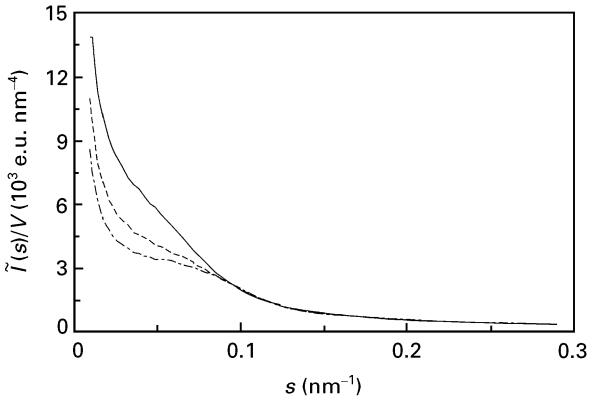

Figure 1 Measured absolute SAXS intensities, $\tilde{I}(s)/V$, of three PET samples crystallized at 4 kbar for 3 h. For clarity, the tails of the measured curves are suppressed in the drawing. (—) D 63 ($\rho = 1.463$ g cm^{-3}), (– – –) D59 ($\rho = 1.459$ g cm^{-3}), (– – – –) D55 ($\rho = 1.455$ g cm^{-3}).

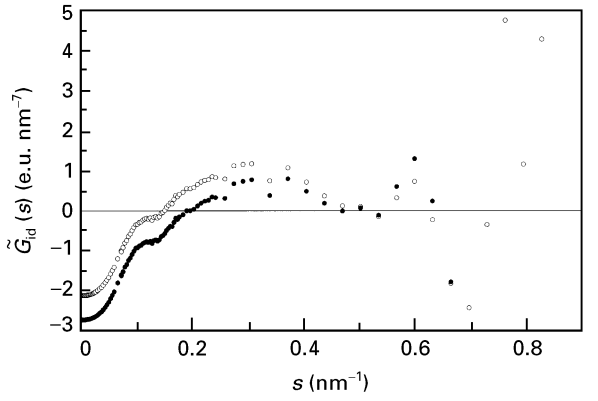

Figure 2 Sample D59: difficulties with the determination of $\tilde{G}_{id}(s)$. Owing to a long-ranging form factor scattering, there remains some freedom for the choice of $\tilde{I}_{Fl}/V$, d_t and $\tilde{A}_P$.

Fig. 2 documents a problem with the determination of the interference function, $\tilde{G}_{id}(s)$, which is common for all three samples: owing to the special structure of the samples, Porod's law does not become valid before $s = 0.45\ nm^{-1}$. For $s > 0.5\ nm^{-1}$, one observes the well-known region where the statistical noise grows because of the properties of the applied transformation (Equation 3), and the region for evaluation according to Porod's law becomes very small. Thus one has some freedom to choose the values for the parameters $\tilde{I}_{Fl}/V$, d_t and Porod's asymptote, $\tilde{A}_P$. On the other hand, the choice of the values of the parameters is constrained by physical reasons. If, for example, $\tilde{I}_{Fl}/V$ is chosen too large, the scattering curve of the corresponding ideal system will show negative values. If $\tilde{I}_{Fl}/V$ is chosen too small, d_t becomes negative. But even in the allowed range there remains some freedom, so that we have to scan the parameter space, compute the interface distribution functions, $g_1(x)$, and analyse the physical meaning of the obtained curves in order to find appropriate values of $\tilde{I}_{Fl}/V$, d_t and $\tilde{A}_P$.

Fig. 3 illustrates this procedure for sample D59: If one chooses a large d_t, one still has some freedom to choose $\tilde{A}_p$ and $\tilde{I}_{Fl}/V$ (cf. Fig. 2). One obtains interface distributions with a pronounced wiggling (dashed curves in Fig. 3). In particular, the depth of the

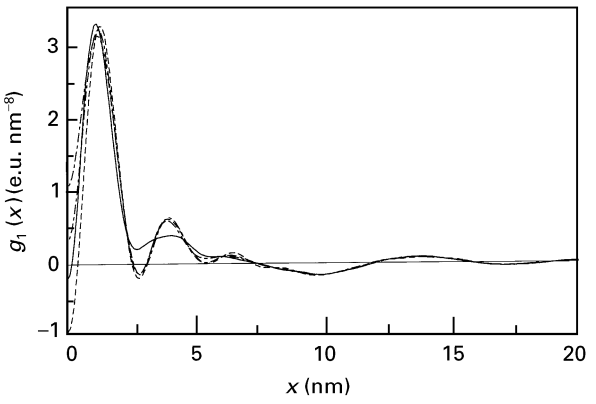

Figure 3 Sample D59: computed interface distributions, $g_1(x)$, for various choices of the parameters $\tilde{I}_{Fl}/V$, d_t and $\tilde{A}_P$. Large values for d_t: $\tilde{A}_P$ = (– –) 2.1, (— — —) 2.5 and (— — —) 2.7 e.u. nm^{-7}. (—); d_t; "small but positive": $A_P = 2.4$ e.u. nm^{-7}.

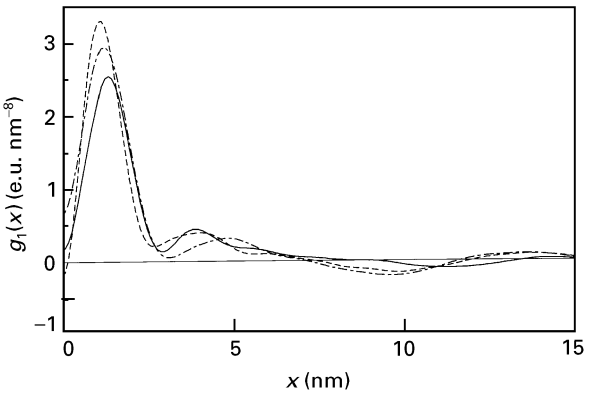

Figure 4 Final IDFs $g_1(x)$ of three high-pressure crystallized PET samples. $g_1(x)$ describes the one-dimensional statistics within the stacks from amorphous and crystalline layers. (—) D63, (– – –) D59, (— — —) D55.

minimum at $r = 6$ nm prevents the curves from being successfully fitted with any reasonable stacking statistics. If, on the other hand, d_t is chosen to be "small but positive", the determination of the interference function is straightforward. One varies $\tilde{I}_{Fl}/V$ until the integral of $\tilde{G}_{id}(s)$ approximately vanishes. Then, one finds the only possible set of parameters and, after transformation, one obtains an interface distribution (solid line in Fig. 3) with only moderate oscillations.

The three observed positive peaks, which appear before the detected "long period peak" with negative sign lead to the conclusion that at least two different kinds of layer stacks with different average layer thicknesses are present. The severe damping shows that the long-range order along the stack of layers, independently from the choice of the parameters $\tilde{I}_{Fl}/V$, d_t and $\tilde{A}_P$, is very poor. Thus the choice of some one-dimensional lattice model appears not to be appropriate. Consequently, the interface distributions have been fitted by two kinds of lamellar stacks, each one corresponding to the paracrystalline model (iii). The results obtained for the three samples are shown in Fig. 4.

Although it seems to be obvious that at least a two-component lamellar system is necessary, if one intends to obtain a reasonable fit, a one-component fit has to be tried as well. An example for the comparison between a single-component fit and a double component fit is shown in Fig. 5. Even with the sample D55, which does not show the three positive peaks, the single-component fit does not appear to be acceptable. If, nevertheless, one assumes a single-component for the fit and compares the specific surface S/V computed from the structural data of the fit with the theoretical value $2/\bar{L}$, one would find $S/V \approx 1/\bar{L}$, which is only half as large as the minimum theoretical value. The double-component fit, on the other hand, yields agreement within the error of determination.

Fig. 6 represents the frequency distributions of layer thicknesses obtained after the composition of the interface distribution of Fig. 5 using the fitting procedure discussed above. In this plot the ordinate has been rescaled and expressed in units of the first derivative of the specific surface, as pointed out in the theoretical section of the Appendix. The distance distributions

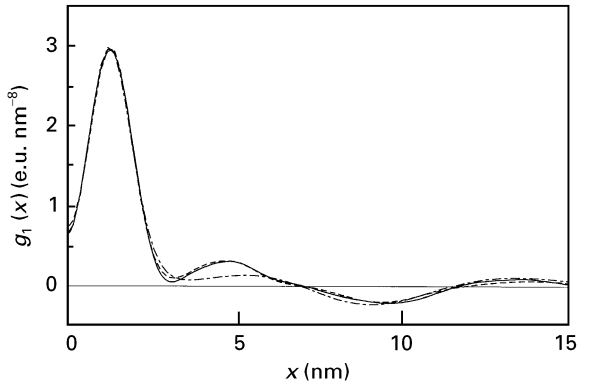

Figure 5 Comparison of (– – – – –) double-component fit versus (— — —) single-component fit on (—) the interface distribution function (IDF) of sample D55.

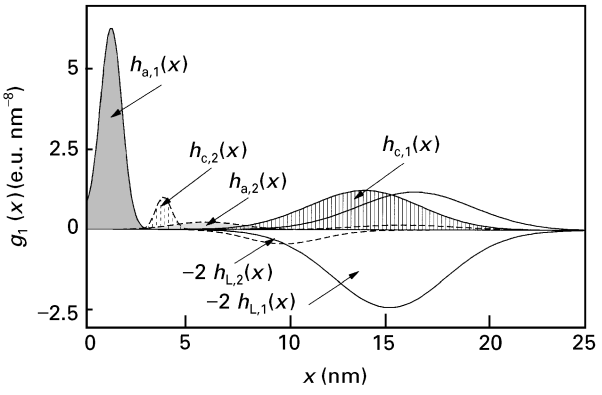

Figure 6 Sample D59: decomposition of the IDF into the series of distance distributions, $h_t(x)$, by a two-component model fit.

$h_{a,1}(x)$ and $h_{a,2}(x)$ represent the thickness distributions of the amorphous layers of the two components, $h_{a,1}(x)$ being related to the dominant component which represents the majority of the layer stacks in the sample. Similarly, $h_{c,1}(x)$ and $h_{c,2}(x)$ represent the thickness distributions of the crystalline layers. The thickness distributions of the long periods $2h_{L,1}(x)$ and $2h_{L,2}(x)$ appear with negative sign. For high values of x one observes two broad distance distributions with positive sign, which are not labelled.

They describe the composite lamellae in the stacks, which are made up of two amorphous layers with a crystalline layer in between. All the thickness distributions of single layers have been shaded using different patterns.

By inspection of the thickness distributions of the single layers one observes that the majority of the stacks possesses an extremely high "linear crystallinity", α_L, while the stacks of the smaller component show a crystallinity of about 40%, which is the customary value for PET [26]. The term "linear crystallinity", $\alpha_L = \bar{d}_c/\bar{L}$, designates the crystallinity within the layer stacks, as determined from the one-dimensional IDF.

Tabel II shows the structural parameters, which have been determined before the quantitative analysis of the IDF has been carried out. The density fluctuation background, $\tilde{I}_{Fl}/V$, is a measure for the short-range fluctuation of the electron density within the sample. The values obtained are the smallest ones ever measured for PET by the authors. In a previous study [1] on PET crystallized at atmospheric pressure we found values close to $\tilde{I}_{Fl}/V \approx 550$ e.u. nm^{-4}. Because the magnitude of the density fluctuations is proportional to the isothermal compressibility [34], this finding is in good agreement with the extremely high hardness values of the high-pressure crystallized samples. The values obtained for $\tilde{A}_P$ describe the ideal lamellar two-phase system, which is built up by layers with rugged surfaces. They will be compared to the weights of the fitted interface distributions. $Q_{id} = (\rho_{el_c} - \rho_{el_a})^2 \alpha_L (1 - \alpha_L)$ is the scattering power (or invariant) of the ideal two-phase system and is computed by integrating the corrected scattering curve over the whole reciprocal space. One observes an increase of Q_{id} with increasing sample density, although one would expect the opposite trend, if a high crystallinity keeps growing while the contrast $\Delta\rho_{el} = \rho_{el_c} - \rho_{el_a}$ remains constant.

Table III presents the structural parameters, which have been obtained from the model fits of the IDFs under the assumption of a two-component stacking structure. It is noteworthy that with increasing density of the sample the weight of the major component is decreasing, while the weight of the minor component is increasing. For the larger component, the thickness of the amorphous layers, $\bar{d}_{a,1}$, is almost constant with a value of only 1.3 nm, while the thickness of the crystalline layers, $\bar{d}_{c,1}$, increases with increasing density. The larger component is responsible for the high average crystallinity of the samples. It is also to be noted that for all samples, and both components, the relative width of the thickness distributions of the amorphous layers is considerably wider than that of the corresponding thickness distributions of the crystalline layers. The $\sigma_i/\bar{d}_i$ values in Table III are not the observed relative widths, because of the skewness of the distributions represented by the parameter σ_H. The observable relative variances, $(\sigma_i/\bar{d}_i)_{obs}$, may be computed from the equation

$$[(\sigma_i/\bar{d}_i)^2_{obs} + 1] = [(\sigma_i/\bar{d}_i)^2 + 1](\sigma_H^2 + 1) \qquad (1)$$

Table IV shows the derived parameters of the two-phase layer structures, which have been computed from the values presented in Tables II and III. Firstly, the long periods and the linear crystallinities, $\alpha_{L,i}$, have been computed from the average layer thicknesses. Then, the approximate volume fractions, Φ_i, have been computed using Equation 17. The specific surfaces, $(S/V)_i$, follow from Equation 14. The expected theoretical values for the specific surfaces of flat and infinitely extended layers, $2\nu_i/\bar{L}_i$, are presented for the sake of comparison. The average linear crystallinity, α_L, has been computed from $\alpha_L = \sum_i \Phi_i \alpha_{L,i}$, and the contrast follows from

$$\Delta\rho_{el} = \{Q_{id}/[\alpha_L(1 - \alpha_L)]\}^{1/2} \qquad (2)$$

One observes that the long periods of both components increase with increasing sample density. The volume fraction of the larger component decreases from 95% to 90%, while its crystallinity increases from 87% to 91%. These changes, however, are close to the accuracy of the experiment. The study of the specific surfaces supports the notion of flat and extended layers, whose stacks fill the volume completely. For the smaller component the crystallinity decreases with increasing sample density. For this component it could be possible to exchange the assignment of the

TABLE II Structural parameters determined directly from the slit-smeared SAXS data of three high-pressure crystallized PET samples: density fluctuation background, $\tilde{I}_{Fl}/V$, Porod's asymptote, $\tilde{A}_P$, and total scattering power, Q_{id}, of the ideal two-phase system. The thickness of the phase transition zone, d_t, is assumed to be very narrow. Under this assumption the error bars cover the range of meaningful parameter variation

	D55	D59	D63
$\tilde{I}_{Fl}/V$ (e.u. nm^{-4})	259 ± 7	253 ± 7	264 ± 7
$\tilde{A}_P$ (e.u. nm^{-7})	2.5 ± 0.2	2.4 ± 0.2	2.1 ± 0.2
Q_{id} (e.u. nm^{-6})	244.7 ± 3	254.9 ± 13	273.1 ± 13

TABLE III Structural parameters determined from two-component model fits on the IDF. The numerical index discriminates between the different components. W_1 and W_2 are the weights of the components; $\bar{d}_a$ and $\bar{d}_c$ are the average thicknesses of the amorphous and crystalline layers, respectively; $\sigma_a/\bar{d}_a$ and $\sigma_c/\bar{d}_c$ are the relative variances of the local thickness distributions, and σ_H is the heterogeneity of the sample. The error bars are asymptotic intervals of confidence, as computed by the fit program from the parameter correlation matrix

	D55	D59	D63
Larger component:			
W_1(e.u. nm^{-7})	9.29 ± 0.05	8.61 ± 0.06	7.27 ± 0.04
$\bar{d}_{a,1}$ (nm)	1.29 ± 0.01	1.26 ± 0.01	1.48 ± 0.01
$\bar{d}_{c,1}$ (nm)	8.8 ± 0.2	11.1 ± 0.5	14.2 ± 0.7
$\sigma_{a,1}/\bar{d}_{a,1}$	0.45 ± 0.01	0.375 ± 0.006	0.31 ± 0.07
$\sigma_{c,1}/\bar{d}_{c,1}$	0.13 ± 0.01	0.18 ± 0.03	0.01
$\sigma_{H,1}$	0.21 ± 0.01	0.17 ± 0.01	0.28 ± 0.07
Smaller component:			
W_2(e.u. nm^{-7})	0.55 ± 0.03	1.01 ± 0.04	1.15 ± 0.05
$\bar{d}_{a,2}$ (nm)	3.5 ± 0.1	5.1 ± 0.1	7.2 ± 0.2
$\bar{d}_{c,2}$ (nm)	4.69 ± 0.05	3.86 ± 0.04	4.27 ± 0.08
$\sigma_{a,2}/\bar{d}_{a,2}$	0.39 ± 0.06	0.33 ± 0.03	0.28 ± 0.04
$\sigma_{c,2}/\bar{d}_{c,2}$	0.09 ± 0.02	0.16 ± 0.01	0
$\sigma_{H,2}$	0.10 ± 0.02	0	0.17 ± 0.03

TABLE IV Derived structural parameters, computed from the values given in the preceding tables. The numerical index discriminates between the different components. Φ is the volume fraction occupied by the ith component. $\bar{L}_i$ is the long period. $\alpha_{L,i}$ is the linear crystallinity from SAXS. S_i/V is the specific surface. $2\Phi_i/\bar{L}_i$ is the expected theoretical value for the specific surface in the case of flat and infinitely extended layers. $\Delta\rho_{el}$ is the electron density difference between the two phases. For the larger component the apparent relative widths, $(\sigma_i/\bar{l}_i)_{obs}$, are presented (cf. Equation 1). The intervals of confidence are computed by applying the rules of the error propagation

	D55	D59	D63
Larger component:			
Φ_1	0.954 ± 0.003	0.922 ± 0.004	0.896 ± 0.006
$\bar{L}_1$ (nm)	10.1 ± 0.2	12.4 ± 0.3	15.7 ± 0.7
$\alpha_{L,1}$	0.87 ± 0.03	0.90 ± 0.05	0.91 ± 0.06
S_1/V(m^2 cm^{-3})	182 ± 27	159 ± 49	134 ± 40
$2\Phi_1/\bar{L}_1$(m^2 cm^{-3})	189 ± 4	149 ± 7	114 ± 6
$(\sigma_a/\bar{l}_a)_{obs}$	0.51 ± 0.01	0.42 ± 0.01	0.43 ± 0.07
$(\sigma_c/\bar{l}_c)_{obs}$	0.25 ± 0.01	0.25 ± 0.03	0.28 ± 0.07
Smaller component			
Φ_2	0.046 ± 0.003	0.078 ± 0.004	0.104 ± 0.006
$\bar{L}_2$ (nm)	8.2 ± 0.2	9.0 ± 0.2	11.5 ± 0.3
$\alpha_{L,2}$	0.57 ± 0.01	0.43 ± 0.01	0.37 ± 0.01
S_2/V(m^2 cm^{-3})	11 ± 2	19 ± 6	21 ± 6
$2\Phi_2/\bar{L}_2$(m^2 cm^{-3})	11 ± 5	17 ± 4	18 ± 4
Sample averages:			
α_L	0.86 ± 0.03	0.86 ± 0.05	0.85 ± 0.05
$\Delta\rho_{el}$(e.u. nm^{-3})	44.9 ± 3	46.2 ± 7	46.3 ± 7

crystalline layers with that of the amorphous layers. This would justify the fact that the average linear crystallinity would increase (0.85 ± 0.03, 0.87 ± 0.05, 0.88 ± 0.04) with increasing density. However, it would present the difficulty that the contrast between the phases should increase beyond the theoretical value for ideal phase separation of 47.5 e.u. nm^{-3} (44 ± 3, 48 ± 8, 50 ± 7). We admit that, because of the low accuracy, the chosen assignment is more or less arbitrary. However, our choice results in a stronger support for the extreme microhardness found in sample D59 (cf. Table I).

5. Discussion

Inspection of the raw scattering curves immediately reveals that the crystalline layers within these high crystalline PET samples possess a short-range order. Further analysis of the SAXS indicates that 90% or more of the sample volume is filled with stacks from crystalline layers with only a narrow amorphous zone in between. The observed thickness of the crystalline layers is extremely high in support of our previous findings [3]. In analogy to studies from the field of metallurgy [4, 6–8] we suggest the observed structure is termed a "layered nanocrystalline structure". In this sense, high-pressure crystallization of PET might be called a venture from the semicrystalline into the nanocrystalline regime.

Within the error of the experiment, the computed electron density contrast yields the theoretical value. Only for sample D55 there is an indication for a reduced contrast, which might indicate a high amount of crystal imperfections. The broad error band of the parameter values predominantly originates from the uncertain determination of the sample thicknesses (the samples splintered when they were cut). The mass density, the crystallinity of the nanocrystalline stacks and the melting point increase simultaneously (Table I) while the fraction of the nanocrystalline stacks decreases (Table IV). The values for the volume crystallinity from DSC, α_{cC}, rise with decreasing microhardness. Both parameters show no correlation with the volume crystallinity from density, α_D. The value of α_D itself remains significantly lower than the linear crystallinity from the SAXS analysis, α_L. One can explain such a finding by the presence of amorphous material outside the lamellar stacks. In a previous paper [28] such kind of material was found in layers which limit the coherence length of the stacks of lamellae. These layer stacks were shown to contain only a few coherently scattered crystalline lamellae. A determination of the stack height from the data from the present samples is cumbersome (if not unreasonable) because of the implications caused by the distinct form factor scattering of the thin amorphous layers.

Unexpectedly, the highest microhardness value was not obtained for the sample with the highest density, but for the sample D59. According to the SAXS analysis, D59 is the sample with the highest linear crystallinity and with the narrowest amorphous layers within the major component stacks. In addition, with respect to the width of the layer thickness distributions in the nanocrystalline component (cf. Table IV), sample D59 is more perfect than the other ones. On the other hand, the linear crystallinity of the nanocrystalline regions of sample D59 is close to that of the sample D63. Hence, the low hardness value obtained for sample D63 may be sought in the thicker amorphous layers and in the decreased nanocrystalline fraction.

The microhardness value of PET crystallized at atmospheric pressure [1] is about 60% lower than that of the nanocrystalline material [3] investigated in the present study. For sample D59 the measured microhardness is even higher than that for the prediction of infinitely thick crystals from *ab initio* calculations [35], $H_c^\infty = 380$ MPa. The decrease of microhardness with decreasing crystal thickness is a general phenomenon for semicrystalline polymers crystallized under atmospheric pressure and is explained by the surface free energy influence [36]. Why does this effect not occur in our samples? We believe that this is due to the fact that the amorphous layers are very thin. To a first approximation one could conclude that such thin layers do not decrease the microhardness. Furthermore, it might be useful to consider the Hall–Petch relation [5, 37]

$$\sigma = \sigma_0 + \frac{f}{d_c^{1/2}} \tag{3}$$

according to which the observed yield stress, σ, can be larger than the lattice friction stress required to move individual dislocations, σ_0. d_c is the size of the crystalline grain and f is a constant. Through Tabor's relation, σ and σ_0 correspond to H_c and H_c^∞, respectively [35]. This relation is only applicable if the amorphous

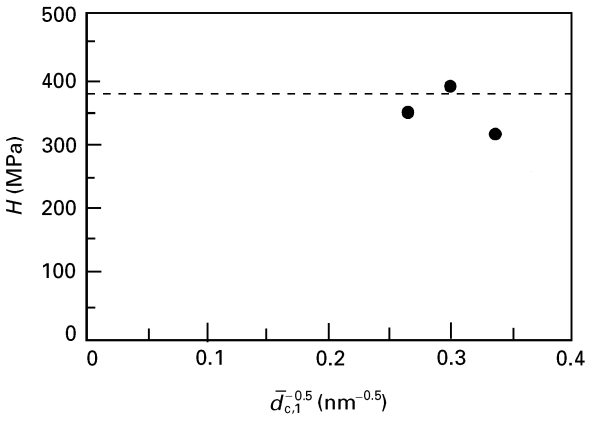

Figure 7 Hall–Petch plot from the microhardness values, H, and the crystalline layer thickness of the nanocrystalline component, $\bar{d}_{c,1}$, for three PET samples crystallized at 4 kbar for 3 h. (———) The level of the calculated hardness for infinitely thick crystals.

zones are thin enough to be considered as mere grain boundaries. It is a peculiarity of the nanocrystalline regime, that due to the small size, d_c, of the crystallites, a considerable increase of the microhardness beyond the theoretical microhardness of the single crystal can be predicted. Experimental data for layered nanocomposites, which support this prediction are published in the review of Froes and Suryanarayana [4]. From our data of Fig. 7, it is difficult, however, to draw any clear dependence of H upon $\bar{d}_{c,1}$. According to Hall–Petch predictions, sample D55 should show the highest microhardness value while, in fact, it presents the lowest H value. In order to explain this shortcoming, one may consider the lower density and small contrast of this sample and may speculate about the amorphous material which might sandwich the layer stacks and, consequently, reduce the microhardness values.

6. Conclusion

By crystallizing PET at high pressure, a material with nanocrystalline structure, consisting of crystalline lamellae with a thickness of approximately 10 nm separated by thin amorphous layers (< 1.5 nm), has been prepared. Such a material has not been obtained with any polymer crystallized under normal conditions where the amorphous layers usually are larger than 2 nm. The nanocrystalline structure is related to an unexpectedly high value of microhardness. This method of preparation could be a promising technique for the development of other nanocrystalline polymeric materials with conducting, ferroelectric and optical properties having enhanced mechanical behaviour.

Acknowledgements

Thanks are due to the DGICYT Spain (Grant PB-94-0094) for support of this investigation. One of us (F.J.B.C.) also thanks the Alexander von Humboldt Stiftung, Bonn for the Humboldt Award by which this work was also supported. The authors gratefully acknowledge the preparation of the samples by O. Öhm.

Appendix. Theoretical considerations

A.1. The interface distribution function

The absolute slit-smeared scattering intensity, normalized with respect to the primary beam intensity, geometrical factors and the scattering volume, V, will be designated by $\tilde{I}(s)/V$ and is obtained in units of e.u. nm^{-4}. Here $s = (2\lambda)\sin\theta$, λ being the wavelength of radiation and θ being half the scattering angle. The investigated samples consist of crystalline and amorphous regions connected by transition zones of finite thickness and showing a short-range local density fluctuation within each of the regions. Let $\tilde{I}_{id}(s)/V$ be the slit-smeared scattering curve of the corresponding ideal two-phase system without density fluctuations and with sharp phase boundaries, and let it be sufficient to describe the deviations of the investigated system from the ideal one by only two scalar parameters $\tilde{I}_{Fl}/V$ and d_t. $\tilde{I}_{Fl}/V$ is a constant background intensity, which takes into account the local density fluctuations within each of the two phases, and d_t is the thickness of the transition zone between the phases (the limitation of this rough approximation has been extensively discussed in previous papers [7, 8]). Then $\tilde{I}_{id}(s)/V$ describes the scattering of a sample, for which the electron density, $\rho_{el}(\boldsymbol{r})$, at every point r in the irradiated volume V can only take one of two values. $\rho_{el}(\boldsymbol{r})$ shows a discontinuity at the phase boundary. This phase boundary forms the inner surface of the sample, occupying no volume. In such an ideal two-phase system, the volume is divided into two disjunct regions, and structure investigation remains only a matter of two-phase topology and of weighting factors.

Furthermore, let us assume that the regions of the two phases are arranged in the form of stacked layers with sufficiently large lateral extension and let us define in real-space a coordinate, x, which runs through the stacks in the direction perpendicular to the layer surfaces. The scattered intensity $\tilde{I}_{id}(s)/V$ of such a one-dimensional ideal system only is a function of the statistics of the distances, d_{ij}, between any pair of phase boundaries labelled i and j along the stack (where the sign of each contribution has to be taken into account). In this context, the symbol d is used for distances in the one-dimensional system, whereas the letter l will be used for solid angle averages of distances.

According to Ruland [24, 38] it is useful to transform the smeared scattered intensity of the observed two-phase system, $\tilde{I}(s)/V$, into the so-called interference function of the ideal two-phase system, $\tilde{G}_{id}(s)$, by means of the equation

$$\tilde{G}_{id}(s) = \frac{[\tilde{I}(s)/V - \tilde{I}_{Fl}/V]s^3}{(1 - 8\pi^2\sigma_t^2 s^2)\ \mathrm{erfc}(2\pi\sigma_t s) + 4(\pi\sigma_t s)^{1/2}\exp(-4\pi^2\sigma_t^2 s^2)} - \tilde{A}_P. \quad \text{(A1)}$$

where $\sigma_t = d_t/3$ is a measure of the width of the transition zone between the phases, and $\tilde{A}_P$ is the Porod's asymptote of the slit-smeared scattering curve, $\tilde{I}(s)/V$ (in the case of an ideal system the smeared scattering intensity, $\tilde{I}_{id}(s)/V$, for sufficiently large values of s, is given by $\tilde{A}_P/s^3$). The parameters $\tilde{I}_{Fl}/V$, d_t and $\tilde{A}_P$ in this representation are determined by a fitting procedure [28]. By transforming $\tilde{G}_{id}(s)$ from reciprocal into real space, the interface distribution function (IDF), $g_1(x)$, is obtained

$$g_1(x) = \pi \int_0^\infty \tilde{G}_{id}(s) \left[4J_0(2\pi xs) - 2\left(2\pi xs + \frac{1}{2\pi xs}\right) \times J_1(2\pi xs) \right] ds \quad \text{(A2)}$$

where J_0 and J_1 are Bessel functions of orders zero and one. (Compared to earlier definitions, two changes have been made: higher order Bessel functions have been expressed in terms of lower order ones, and the normalization has been changed, so that now $\int_{-\infty}^{\infty} g_1(x)dx = A_{P_1}$ (instead of $\tilde{A}_P$); for definitions cf. Equations 7 and 8). $g_1(x)$ is proportional to the second derivative of the one-dimensional correlation function [23]. The IDF is composed of a series of distance distributions, $h_i(x)$. The centres of gravity of the first two distance distributions, $\bar{d}_1$ and $\bar{d}_2$, represent the average thicknesses of the layers of phase 1 and phase 2, respectively. The average is taken over the irradiated volume. For many semicrystalline systems it is easy to identify which one of the two values is the average thickness of the amorphous and which one is the average thickness of the crystalline layers.

A.2. The weight of the interface distribution in absolute units

In many cases one can assume that the slit of the Kratky camera is infinitely long. This means that the well-known smearing equation

$$\tilde{I}(s)/V = 2\int_0^\infty I(s^2 + y^2)^{1/2}/V dy \quad \text{(A3)}$$

is valid, with $I(s)/V$ being the scattered intensity, which one would measure with a point focus. Let the scattering arise from layer stacks with sufficiently flat and extended surfaces. In this case it is useful to define a one-dimensional intensity, $I_1(s)/V$, which could be directly measured if all the lamellar stacks had the same orientation. $I_1(s)/V$ and $I(s)/V$ are related by

$$I_1(s)/V = 2\pi s^2 I(s)/V \quad \text{(A4)}$$

With the limiting values for the corresponding Porod's law being defined as

$$A_{P_1} = \lim_{s\to\infty} s^2 I_1(s)/V \quad \text{(A5)}$$

$$\tilde{A}_P = \lim_{s\to\infty} s^3 \tilde{I}(s)/V \quad \text{(A6)}$$

$$A_P = \lim_{s\to\infty} s^4 I(s)/V \quad \text{(A7)}$$

and with Equations A3 and A4 one finds

$$A_{P_1} = 4\tilde{A}_P = 2\pi A_P \quad \text{(A8)}$$

The quantity A_P is given in units of e.u nm^{-7}. (In a preceding paper [17], A_P was incorrectly given in e.u. nm^{-8} units. Moreover, in the former paper, the symbol A_P has been used instead of A_{P_1}).

Using Equations A1 and A2 it can be shown that

$$\begin{aligned} A_{P_1} &= 2\int_0^\infty g_1(x)\, dx \\ &= 2\int_0^\infty h_1(x)\, dx \\ &= 2\int_0^\infty h_2(x)\, dx \end{aligned} \quad \text{(A9)}$$

where $h_1(x)$ and $h_2(x)$ represent the thickness distribution of the crystalline and the amorphous layers, respectively. Thus the Porod constant which can be determined fitting the tail of the curve $I_1(s)s^2/V$ is also equal to the total integral of the IDF. Therefore, Porod's invariant A_{P_1} can also be called the weight of the IDF $g_1(x)$ and will be designated by the symbol W.

In order to determine the thickness distributions $h_1(x)$ and $h_2(x)$ from the measured IDF, one firstly has to define a mathematical model of the IDF which describes the statistics of stacked lamellae and secondly has to vary the parameters of this model until the resulting model function fits the measured IDF. It is interesting to compare W_{fit}, the value for the parameter, W, obtained by the fit, with the measured value $W_{mea} = A_{P_1}$. If one chooses a model in which the lamellae building up the ideal system are completely flat, it might turn out that a fitting for small values of x (the values left of the first maximum) is not possible. Here the fitted values may be smaller than the measured ones, so that

$$W_{fit} \leqslant W_{mea} \quad \text{(A10)}$$

This means that there exist some very small additional crystalline and/or amorphous regions, which were not taken into account in the model based on flat lamellae. These additional regions can only be built up by bulges and/or dips in the surface of the lamellae thus giving rise to a rugged phase boundary [28, 29, 39, 40]. Therefore a comparison of W_{fit} with W_{mea} can reveal important information on the smoothness of the inner surface.

A.3. The inner surface of the lamellar two-phase system

An ideal lamellar system with perfect and infinitely extended layers will show two surfaces per long period, $\bar{L} = \bar{d}_1 + \bar{d}_2$. Therefore, its specific surface S/V is given by

$$\frac{S}{V} = \frac{2}{\bar{L}} \quad \text{(A11)}$$

For an ideal two-phase system, $W_{mea} = A_{P_1}$ may be expressed in terms of the contrast between the two

phases, $\Delta\rho_{el} = \rho_{el_1} - \rho_{el_2}$ and the specific surface [41]

$$W_{mea} = \frac{\Delta\rho_{el}^2}{4\pi^2}\frac{S}{V} \tag{A12}$$

Thus it is possible to compute the specific surface from the Porod's asymptote, if the electron density difference between the two phases is known. If one compares a computed value for S/V with the theoretical value $2/\bar{L}$, one should compute S/V from W_{fit} rather than from A_{P_1} (cf. Section A.2: $W_{mea} = A_{P_1}$ may contain a contribution from the roughness of the layer surfaces).

A.4. A multi-component lamellar system and the volume fractions of its components

When analysing the SAXS, sometimes it becomes necessary to assume that two kinds of lamellar stacks showing different structural parameters (long period, crystallinity, layer statistics) coexist. From this it follows that each component i has its own weight W_i which, according to the above considerations, is the partial Porod's asymptote of the ideal and smooth layer system with respect to the one-dimensional scattering intensity. Generally, for a system with i components, Equation A12 has to be replaced by a set of i equations

$$W_i = \frac{(\Delta\rho_{el}^2)_i}{4\pi^2}\frac{S_i}{V} = \frac{(\Delta\rho_{el}^2)_i}{4\pi^2}\left(\frac{S}{V}\right)_i \Phi_i, \tag{A13}$$

with Φ_i being defined as the fraction of volume, which is filled by the ith kind of stacks. The values of the W_i can be determined in a non-linear regression analysis by fitting the parameters of an IDF model with two kinds of stacks to the observed IDF.

It is of some interest to estimate the values of the Φ_i. Neglecting the effect of bent layers, one may approximate

$$\left(\frac{S}{V}\right)_i = \frac{S_i}{V\Phi_i} \approx \frac{2}{\bar{L}_i} \tag{A14}$$

where $\bar{L}_i$ is the long period of the ith component. If, moreover, W_i is the Porod's asymptote of the smooth system, and if one assumes that the contrast between the phases is the same within the different kinds of layer stacks, one finds

$$\Phi_i \approx \frac{\bar{L}_i W_i}{\sum_j \bar{L}_j W_j} \tag{A15}$$

Thus, under the above approximations, the volume fraction Φ_i of the ith component in a multi-component layer system is proportional to the product of its long period and its weight in the interface distribution function.

References

1. C. SANTA CRUZ, F. J. BALTÀ CALLEJA, H. G. ZACHMANN, N. STRIBECK and T. ASANO, *J. Polym. Sci. Polym. Phys.* **B29** (1991) 819.
2. C. SANTA CRUZ, N. STRIBECK, H. G. ZACHMANN and F. J. BALTÀ CALLEJA, *Macromolecules* **24** (1991) 5980.
3. F. J. BALTÀ CALLEJA, O. ÖHM and R. K BAYER, *Polymer* **35** (1994) 4775.
4. F. H. FROES and C. SURJANARAYANA, **41** (1989) 12.
5. J. R. WEERTMAN, *Mater. Sci. Eng.* **A166** (1993) 161.
6. H. GLEITER, *Progr. Mater. Sci.* **33** (1989) 223.
7. R. BIRRINGER, *Mater. Sci. Eng.* **A117** (1989) 33.
8. C. N. J. WAGNER, *J. Non-Cryst. Solids* **150** (1992) 1.
9. K. LU, J. T. WANG and W. D. WEI, *J. Appl. Phys.* **69** (1991) 522.
10. K. LU, R. LÜCK and B. PREDEL, *Acta Metall. Mater.* **42** (1994) 2303.
11. H. R. HILZINGER and H. WARLIMONT, *Sci. Am.* (*German ed.*) **7** (1994) 108.
12. J. LIPOWITZ, J. A. RABE, G. A. ZANK, Y. XU and A. ZANGVIL "Nanocrystalline silicon carbide fibers derived from organosilicon polymers" in Chemical Processes in Advanced Materials edited by L. L. Hench and J. K. West (Wiley, New York, 1992) p. 767.
13. Z. F. ZHANG, F. BABONNEAU, R. M. LAINE, Y. MU, J. F. HARROD and J. A. RAHN, *J. Am. Ceram. Soc.* **74** (1991) 670.
14. J. LIPOWITZ, J. A. RABE, L. K. FREVEL and R. L. MILLER, *J. Mater. Sci.* **25** (1990) 2118.
15. T. ERNY, M. SEIBOLD, O. JARCHOW and P. J. GREIL, *J. Am. Ceram. Soc.* **76** (1993) 207.
16. J. K. VASSILIOU, V. MEHROTRA, M. W. RUSSELL, E. P. GIANNELIS, R. D. McMICHAEL, R. D. SHULL and R. F. ZIOLO, *J. Appl. Phys. Part* 1 **73** (1993) 5109.
17. T. HIRAGA, N. TANAKA, K. HAYAMIZU, A. MITO, S. TAKARADA, Y. YAMASAKI, M. NAKAMURA, N. HOSHINO and T. MORIYA, *Jpn J. App. Phys. Part* 1 **32** (1993) 1722.
18. M. MUKHERJEE, A. DATTA and D. CHAKRAVORTY, *Appl. Phys. Lett.* **64** (1994) 1159.
19. D. GALLAGHER, W. E. HEADY, J. M. RACZ and R. N. BHARGAVA, *J. Crystal Growth* **138** (1994) 970.
20. S. GUHA, G. HENDERSHOT, D. PEEBLES, P. STEINER, F. KOZLOWSKI, W. LANG, *Appl. Phys. Lett.* **64** (1994) 613.
21. H. S. NALWA, H. KASAI, S. OKADA, H. OIKAWA, H. MATSUDA, A. KAKUTA, A. MUKOH and H. NAKANISHI, *Adv. Mater.* **5** (1993) 758.
22. F. J. BALTÀ CALLEJA and C. G. VONK, "X-Ray Scattering of Synthetic Polymers" (Elsevier, Amsterdam 1989) p. 18.
23. C. G. VONK and G. KORTLEVE, *Coll. Polym. Sci.* **220** (1967) 19.
24. W. RULAND, *ibid.* **255** (1977) 417.
25. D. J. BLUNDELL and D. N. OSBORN, *Polymer* **24** (1983) 953.
26. R. GEHRKE and H. G. ZACHMANN, *Makromol. Chem.* **182** (1981) 627.
27. S. POLIZZI, N. STRIBECK, H. G. ZACHMANN and R. BORDEIANU, *Coll. Polym. Sci.* **267** (1989) 281.
28. N. STRIBECK, *ibid.* **271** (1993) 1007.
29. N. STRIBECK, R. G. ALAMO, L. MANDELKERN and H. G. ZACHMANN, *Macromolecules* **28** (1995) 5029.
30. F. ZERNIKE and J. A. PRINS, *Z. Phys.* **41** (1927) 184.
31. R. HOSEMANN, *ibid.* **128** (1950) 1.
32. *Idem*, *ibid.* **128** (1950) 465.
33. D. J. BLUNDELL, *Polymer* **19** (1978) 1258.
34. J. RATHJE and W. RULAND, *Coll. Polym. Sci.* **254** (1976) 358.
35. F. J. BALTÀ CALLEJA, *Adv. Polym. Sci.* **66** (1985) 117.
36. *Idem*, *Trends Polym. Sci.* **2(12)** (1994) 419.
37. A. H. CHOKSHI, A. ROSEN, J. KARCH and H. GLEITER, *Scripta Metall.* **23** (1989) 1679.
38. W. RULAND, *J. Appl. Crystallogr.* **4** (1971) 70.
39. *Idem*, *Macromolecules* **20** (1987) 87.
40. A. N. SEMENOV, *ibid.* **27** (1994) 2732.
41. L. A. FEIGIN and D. I. SVERGUN "Structure Analysis by Small-Angle X-Ray and Neutron Scattering" (Plenum Press, New York, 1987) p. 53.

Received 15 February 1995
and accepted 2 July 1996